AIAA JOURNAL
Vol. 47, No. 10, October 2009

Shock-Train Structure Resolved with Absorption Spectroscopy Part 2: Analysis and CFD Comparison

Chadwick D. Lindstrom,* Doug Davis,† and Skip Williams‡
U.S. Air Force Research Laboratory, Wright-Patterson Air Force Base, Ohio 45433
and
Chung-Jen Tam§
Taitech, Inc., Beavercreek, Ohio 45430

DOI: 10.2514/1.41077

Multiple-line-of-sight tunable diode laser absorption measurements of the shock-train structure inside a model scramjet isolator are described. Understanding the shock train is important when considering the design of isolators to prevent unstart as well as dealing with heat transfer. Results from experimental studies such as this one can be used to help refine and validate the computational fluid dynamics models that are used in isolator design. Interpretation of the data collected is complicated because of the unsteady nature of the shock train. First, the gigabytes of acquired data are integrated on a scan-by-scan basis to form absorption-versus-time plots that can be used to determine the shock oscillation power spectrum and amplitude. The shock train is found to oscillate about its mean position with a peak-to-peak amplitude nearly equal to the equivalent duct diameter of 5.75 cm and with a power spectrum largely confined below 100 Hz. Next, developing an understanding of fundamental features of the flow requires that some form of intelligent feature extraction is used. This is difficult because the flow features are not simply periodic but involve a multitude of frequencies. Here, *k*-means data clustering is used to reduce the information to shock structures corresponding to various shock-front locations in the scramjet isolator as a function of backpressure. These clustered data sets are then used to extract path-averaged (transverse direction) static temperatures, static pressures, and water concentrations as a function of streamwise position that can be compared with path-averaged computational fluid dynamics computations. The results indicate that the computational fluid dynamics overestimates the shock spacing by 45% and that the path-averaged temperatures and pressures show a factor-of-2 variation more than indicated by the computational fluid dynamics simulations. These results can be used to help improve the computational fluid dynamics computations of the shock-train structure.

I. Introduction

THE previous paper [1] described the design, testing, and initial experimental results of a test campaign to measure the static pressure, static temperature, and density variations in a supersonic shock train of a model scramjet isolator using diode laser absorption. This experiment used 16 different lines of sight (LOS) to probe a region of 7.62 cm (3 in.) in length inside the isolator using three different spectral regions (1391.8, 1392.6, and 1396.4 nm) of the $\nu_1 + \nu_2$ vibrational band of water. In the previous paper, only the flow results with no backpressure were shown, because the goal was to compare the tunable diode laser absorption system (TDLAS) results with either pressure transducer measurements or to reasonably accurate flow simulations (static temperature). This was done to assess the overall accuracy and precision of the TDLAS system. Here, the goal is to characterize the shock-train structure in terms of its oscillation frequencies and oscillation amplitude, as well as to determine streamwise profiles of the shock-train structure for static pressure, temperature, and water concentration. The oscillation frequencies determined will be very different from a single-point transducer because the motion of the shock front is what is being measured, not the variation at a single point of temperature, pressure, or absorption. The streamwise profiles that are obtained are unique, because (unlike wall measurements, which are blurred due to boundary-layer effects) the TDLAS results are indicative of the in-stream flow conditions.

The layout of this paper, to help address the issues raised in the first paragraph, is as follows. First, for completeness so that the reader does not have to always flip back to references in Part 1 [1], the first section gives a brief overview of the experimental setup. Next, the automated data analysis algorithm that is used to compute peak areas from the large volume of raw data is described. Because the algorithm integrates single scans of data (1 ms in duration), the quality of these scans is shown and the process used to expel outlier spectra is described. Because the algorithm uses a single Voigt line shape to represent composite line shapes, the accuracy of the algorithm is revisited using the same simulation technique as Part 1, but for prototypical changes in pressure and temperature found in a shock structure. Finally, the data processing section ends with the absorption-versus-time plot, which shows the shock-train motion through the observation window in the isolator. The data processing section is then followed by an analysis of the power spectrum of the shock-train oscillations, the amplitude of the fluctuations, and their comparison with literature.

The final two sections focus on obtaining the streamwise profiles of static pressure, temperature, and water concentration as a function of backpressure. Although it is possible to look at single-scan results at particular instants in time, optical turbulence (wander and/or diffusion of laser light due to density and/or temperature gradients) as well as the volume of the data set make it difficult to draw good conclusions about the shock structure without averaging. It is therefore necessary to use techniques that will automatically sort the data into similar flow features that can be averaged together. This also significantly improves the signal-to-noise ratio and enables more precise determination of flow properties. Here, *k*-means data

Received 17 September 2008; revision received 12 May 2009; accepted for publication 26 May 2009.

*National Research Council Postdoctoral Fellow, Propulsion Directorate, Aerospace Propulsion Division. Member AIAA.
†Senior Research Engineer, Principal Research Physicist, Propulsion Directorate, Aerospace Propulsion Division. Senior Member AIAA.
‡Principle Research Physicist, Propulsion Directorate, Aerospace Propulsion Division. Senior Member AIAA.
§Senior Research Scientist. Associate Fellow AIAA.

clustering [2] is employed to find these fundamental flow features. This use of *k*-means data clustering shares some similarities with prior work that has used pattern-factor analysis to characterize temperature nonuniformity in gas-turbine engines, and such approaches are becoming more important when interpreting the large time-varying data sets generated by diode-laser-absorption-based diagnostics. After the data clustering has been performed, it becomes possible to compute path-averaged static temperature, density, and pressure from the absorption data. These results are then compared with computational fluid dynamics (CFD) simulations through numerically computing the path-averaged results.

II. Experimental Overview

A brief review of the experimental geometry is given here. Figure 1 shows the experimental setup and the direct-connect test facility of research cell 18 at U.S. Air Force Research Laboratory (AFRL), Propulsion Directorate, Aerospace Propulsion Division (RZAS). The direct-connect test facility consists of a natural-gas-fueled vitiator (1), interchangeable facility nozzle (2), modular isolator (3), modular combustor (not shown), and a 3.5 psia continuous-flow exhaust system (7). For the current study, the combustor was removed and replaced with a large valve (6) that was used to simulate the pressure rise associated with combustion. The TDLAS hardware was attached to the isolator through purge boxes that eliminate ambient water in the portion of the paths outside the flow region, and the beams were projected into the isolator through quartz windows.

Figure 2 shows a view of the measurement plane with the 16 LOS being used to measure the shock train. The flow direction is from left to right and the measurement plane lies at midheight in the isolator in the third direction. As the reader can see from Fig. 2, the setup consists of 14 LOS nearly oriented perpendicular to the streamwise

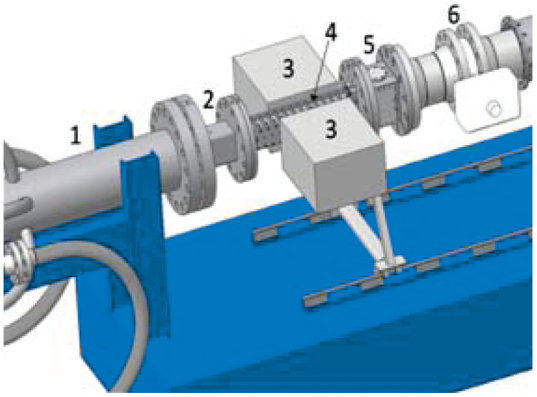

a)

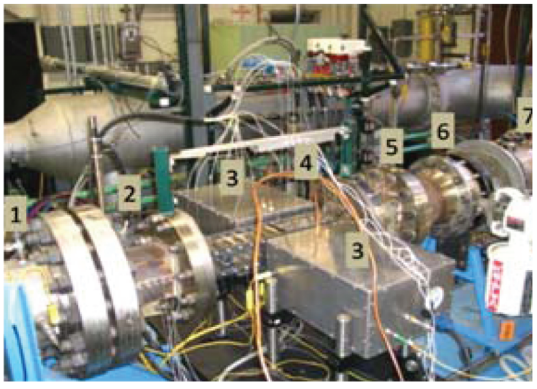

b)

Fig. 1 Supersonic combustion test facility: a) schematic and b) photograph indicating 1: vitiator, 2: facility nozzle, 3: TDLAS hardware, 4: isolator, 5: extension, 6: backpressure valve, and 7: exhaust line.

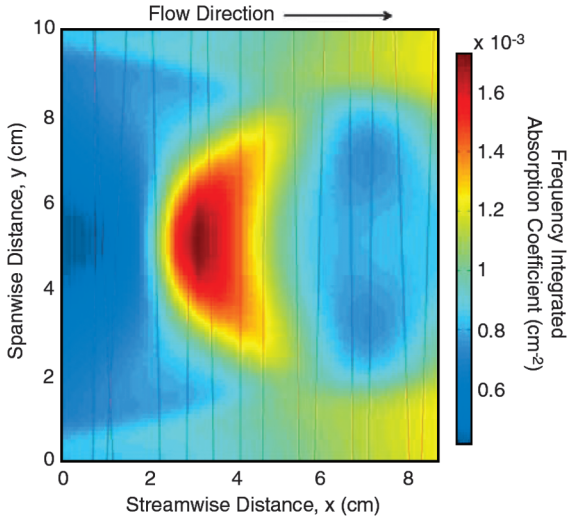

Fig. 2 The 14 lines of sight that are used to probe the 8-cm-long window region in the isolator superimposed on a shock structure generated from a CFD simulation. The measurement plane is at midheight inside the isolator.

x flow direction. The reason that this layout was chosen was that the streamwise direction is the one with the most significant variations in pressure, temperature, density, and velocity. Therefore, the 14 LOS spaced approximately 5 mm apart in this direction provide good sensitivity to these changes. The data acquisition system collects data in a semicontinuous fashion as a backpressure valve is slowly closed to push the shock front forward through the isolator. Variations in absorption will be observed as the shock train passes through the window region being probed, due to changes in static temperature, density, and pressure. The reason for this data-collection scheme is that digitizers generate approximately 100 MB/s of raw data. The currently available commercial hardware cannot achieve that data transfer rate to the hard disk. In addition, during the test each 0.2 s sequence of data was processed and an estimate of the flowfield was displayed to the user every 5 s to provide feedback as to the shock position in the window. Therefore, one complete cycle of data acquisition occurred every 5 s and contained 0.2 s of continuously sampled data at 1 kHz for each of the 16 channels.

In this paper, the analysis will focus on four sets of data labeled runs AB, AC, AF, and AG. The vitiator settings as well as the nozzle Mach number, water mole percent, and the Reynolds number for each case are shown in Table 1. The flow facility provides the capability to preheat the air using electric heaters before vitiation or it can be input to the vitiator at ambient temperatures. The remaining increase in total temperature was achieved using the combustion of natural gas. The Reynolds number has been computed using the equivalent duct diameter (5.75 cm) for a rectangular duct with cross section of 3.81×10.16 cm. More details about the experimental setup and run conditions can be found in Part 1 [1].

III. Data Processing

This section focuses on obtaining the absorption peak areas that are needed to determine the shock-train structure in the previous section. The data are processed on a scan-by-scan basis, and so it is important to first illustrate what the signal-to-noise levels are for a single scan and to then describe the algorithm that is used to process the data. Several important points that are addressed are the issues of outliers and the ability to fit composite line shapes with a single Voigt line shape. Finally, the section ends by presenting the absorption-versus-time plot that is an approximate illustration of the change in absorption as the shock train moves through the measurement window.

A typical data set consisted of 30 cycles of 0.2 s continuous data segments that were collected over approximately 2.5 min while the shock train was slowly advanced through the isolator by gradually

Table 1 Run conditions

Run	Incoming air temperature, K	Total temperature, K	Total pressure, psia	Water mole percent, %	Reynolds number
AB	300	667	50	3.03	9.1×10^5
AC	300	1016	50	6.93	4.6×10^5
AF	589	667	50	1.11	9.1×10^5
AG	589	1016	50	4.94	4.6×10^5

closing a control valve to increase the backpressure. Because each LOS was sampled at 2.5 million samples/second with a 14-bit digitizer, the length of the data set is quite large: approximately 600 MB, including the reference and etalon channels. One approach toward dealing with these large data sets is to simply time-average the data before processing the TDLAS data. This is what was done in Part 1 [1] when dealing with no shock being present in the window. However, because of the shock-front unsteadiness, this is not possible here. Instead, it was necessary to process these data on a scan-by-scan basis. The first step in the data processing was to generate the absorption spectrum from the raw TDLAS data using the reference and etalon data. Figure 3 shows single-scan data recorded near the shock front for each spectral region being probed. As the reader can see, there is noise present in the data due to several sources: optical turbulence, detector noise, and laser turn-on noise. The figure also shows the residuals from a multipeak constrained Voigt fit that has been used to fit each spectral region. Clearly, the data are of sufficient quality that good estimates of the peak area can be obtained to determine whether the shock is present in the window without the need for averaging.

As previously discussed in Part 1 [1], the processing here is using a single Voigt line shape to approximate a measured spectrum that, in the simplest sense, consists of multiple Voigt peaks because of inhomogeneities in static temperature, pressure, and water concentration along the line of sight. As can be seen in Fig. 3, as well as in Fig. 4, this approximation should be adequate to obtain accurate peak areas. However, the measured path-averaged static temperatures, pressures, and water concentrations can be significantly different from a particular point in the flow. In Fig. 4, the path-averaged static temperature and pressure have been computed from a cross section of the CFD simulation of the shock-train structure. A Boltzmann plot was used to compute the path-averaged temperature from peaks a–d (see Part 1 for line parameters), and the width of line a was used to estimate the path-averaged static pressure. Clearly, the static temperature and pressure are greater in the core region than the path-averaged quantities, as expected. To resolve the spatial variations occurring in the cross section of the shock, either a model of the flow must be assumed or additional LOS must be used. However, it is still possible to compute the path-averaged quantities from the CFD, as done here, and to then compare them with the measurements. This may be the best solution when attempting to validate simulations because of instabilities often due to limited data in tomographic reconstruction.

The next step in this process was to build an automated algorithm that could go through the data file and integrate for each time step the spectra in Fig. 3. There are several issues that must be addressed when designing this automated algorithm. The first is that when using a multipeak Voigt fit the parameter space must be constrained so that the optimization algorithm used does not walk off into a space of unreasonable values. Here, this was done using a standard constrained Voigt peak-fitting routine (Levenburg–Marquadt), available in Igor Pro [3].

A second, and perhaps more important, aspect is that it was discovered that on the order of one out of every several hundred measurements was significantly distorted from the spectra shown in Fig. 3. The most likely cause is that it is associated with significant beam walk when the shock front is oriented across a line of sight. Prior efforts that did not examine single-scan data would probably not observe these effects, because they are rare and time-averaging would eliminate them. However, it was desired for these outlier peaks to be flagged and eliminated from the subsequent analysis. Two different algorithms were used. The first was a nonlinear median filter [4]. All 16 lines of sight were rank-ordered based on their integrated absorbance for the strongest spectral line in each spectral region, and the median value was found. If any of the integrated absorbances

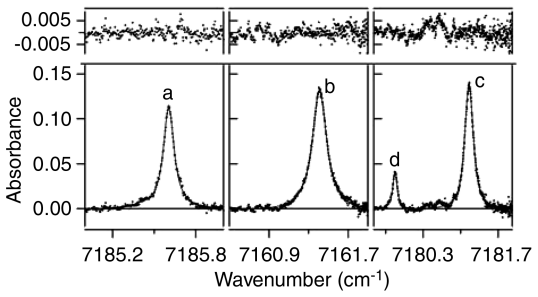

Fig. 3 Single-scan results from the three spectral regions made when the LOS is near a shock front. The data are taken sequentially, with the first spectrum being collected in the first 0.33 ms, the next spectrum in the time bin 0.34–0.66 ms, and the final spectrum at 0.67–1.0 ms. The peak fits (solid black line) and the residuals (upper boxes) are also shown.

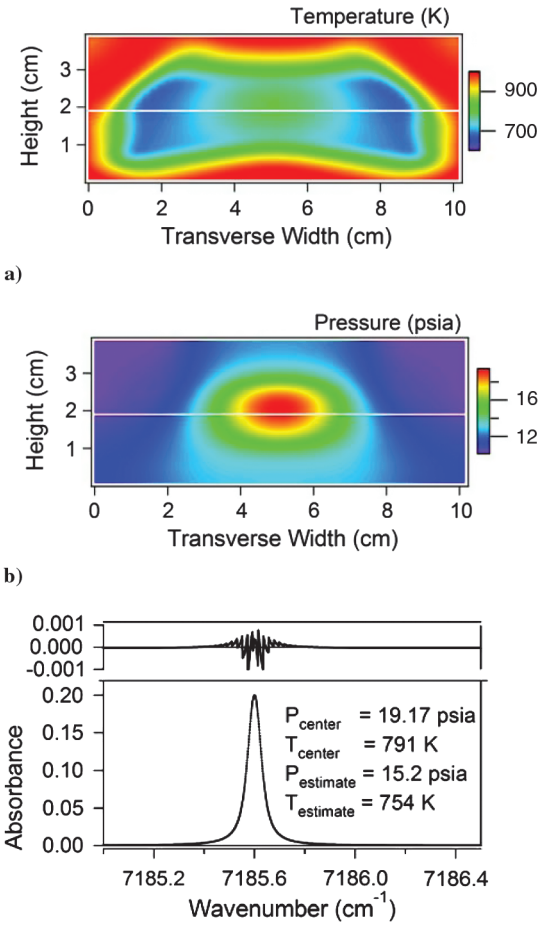

Fig. 4 Pseudo color image of a) static temperature, b) static pressure in the vertical cross section of the isolator when a shock is present (from CFD simulation) along with the LOS, and c) simulated composite line shape and curve-fit residuals from a single Voigt line shape.

exceeded a specified distance from the median value, then that time was specified as an outlier. This procedure was found to be very good at identifying outliers, because if an outlier did occur, only one LOS would usually see it. The second approach was to determine an average chi-square from 40 random samples of the data set. If the chi-square after fitting the peaks exceeded a predetermined threshold, then the particular time was labeled as an outlier. When creating the absorption-versus-time plots, the outlier point was replaced by the median value; however, when performing the data clustering described later, the outlier was simply ignored when creating the cluster average. Another important use of the outlier-detection algorithms was that they provided excellent feedback as to whether the user correctly set up the initial guess parameters for the curve-fitting operations.

A final important aspect of the automated analysis was the speed with which the data could be processed. This represents a significant challenge to the use of large multiplexed TDLAS systems if transient events such as shock-train oscillations are to be measured. The file sizes for the data being processed for this paper ranged from 650 MB–1.35 GB and consisted of 6000–12,000 single-scan measurements. Because of the large file size, the data were broken up into smaller groups that would then be loaded sequentially from the disk. Here, the curve-fitting was the time-limiting step, and it took much longer for the program to compute the curve-fit than the disk reads/writes. It took a HP5750 with an AMD Athlon 64 X2 with 2 GB of RAM approximately 4–8 h to perform the 300,000–600,000 curve fits that were required to generate the absorption-versus-time plots. This time could be significantly lowered through the use of parallel processing, because each LOS could be assigned an individual processor; however, the computational cost was relatively low and so this approach was not used. Because of the time required for computing the data set, it was necessary to make the algorithm fairly robust.

The data from run AB are shown in the grayscale image of Fig. 5. The time axis is shown, with breaks between data segments being represented using a dashed black line, and the axis is labeled based on the scan number within the data set. The data are sampled at 1 kHz rate within each 0.2 s segment, and the segments are separated by approximately 5 s intervals (dotted lines in Fig. 5). Because of the time gaps, the 6000 scans are measured over a time period of 156 s. The x axis is the streamwise position for each line of sight at the center of the isolator referenced to the front of the window (the actual positions can be most easily seen in Fig. 6). The particular absorption line plotted here is the 7185.6 cm^{-1} line described in more detail in Part 1 [1]. This line results from the absorption from a lower state with a ground-state energy of 1045 cm^{-1} and is relatively insensitive to temperature variations in the flow ($T \sim 400$–600 K). Therefore, this plot is fairly indicative of the density variations that are occurring in the flow. As can be seen in the figure, a variety of changes are occurring in the portion of the isolator being probed as time advances. Initially, the leading shock is further downstream of the window and is represented by the white region in Fig. 5. As the shock passes through the window, the absorption increases because of the higher density of the flow, and this region is represented by the black area in the figure. In this particular data set, the facility operator initially closed the backpressure valve too fast and pushed the shock past the window for the times corresponding to scan numbers of 400–600. However, a much slower variation of the backpressure valve, and hence the shock front in the isolator, was achieved from scans from 1800 to 5000. Also shown in Fig. 5 is the outlier plot corresponding to the absorption-versus-time plot. Here, an interesting result is the correlation of the outliers with the position of the shock train in the observation window. If the shock front is either a few inches upstream or downstream of the window, the outlier concentration is almost nonexistent. However, when the shock train is visibly present in the window, the number of outliers increases significantly. This tends to suggest that the presence of outliers is associated with an increase in gross beam walk, due to the presence of the shock front.

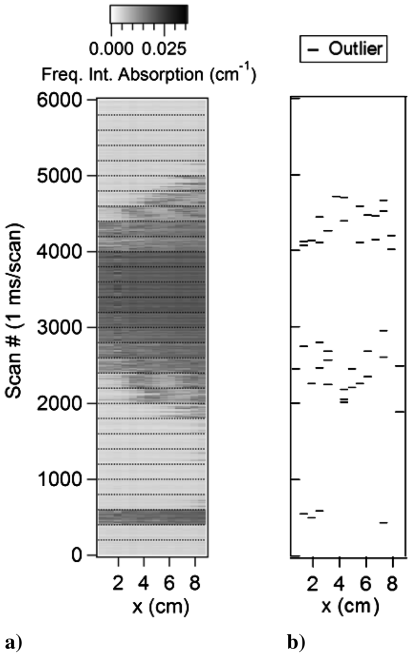

Fig. 5 Plots of a) absorption versus time for the absorption line at 7185.6 cm^{-1} for run AB (dashed lines indicate the 5 s gap between data segments, and so the 6000 scans took approximately 156 s to complete; within each segment the data are sampled at 1 kHz for 200 scans) and b) outlier corresponding to the absorption-versus-time plot.

IV. Time-Resolved Measurements

This section focuses on the temporal variations on the flow. By monitoring multiple lines of sight simultaneously, it is possible to determine the shock-front oscillations and amplitudes. These results are then compared with previous measurements that have been made using more conventional techniques such as high-speed pressure transducers. It should be emphasized here that the measurements follow the shock front and therefore involve multiple lines of sight that track the front location. This is different from conventional measurements that often just measure, for example, static wall pressure at a single location.

Figure 5 shows all of the data for run AB, and the shock is partially in the observation window in multiple time segments. One such segment from 2000–2200 is expanded in Fig. 6. Because it is one data segment, the data were taken continuously at a 1 kHz rate (1 ms scan separation), so that the shock-front oscillations can be observed. Here, the front of the shock train is approximately located at 4 cm and oscillates about that position. Also shown in this figure are two points in time at which the shock is located at similar locations in the window. The profiles are similar, with the frequency-integrated absorption increasing by a factor of 3 from the preshock region to the peak of the first shock.

The solid black line in Fig. 6 was obtained using a peak-finder algorithm. This algorithm works by searching the smoothed first derivative of the data for a zero crossing while also examining the sign of the smoothed second derivative to differentiate between a maximum and minimum. It works well when applied to data in which the first shock is present. However, as can be seen in Fig. 6, at the time of approximately 48 ms (when the beginning of the first shock is no longer present), the algorithm fails at locating the peaks properly. So complete processing of the data set using the peak-finder algorithm is not possible. Instead, in the next section, this problem will be addressed using k-means data clustering.

The shock-front curve allows the frequency content of the shock position to be analyzed. To determine the power spectrum, the mean position is subtracted from the curve and then this relative position curve can then be Fourier-transformed to yield a power spectrum. This is shown in Fig. 7 along with the relative position curve corresponding to the shock front. It should be emphasized here that the power spectrum obtained in this manner is very different from one

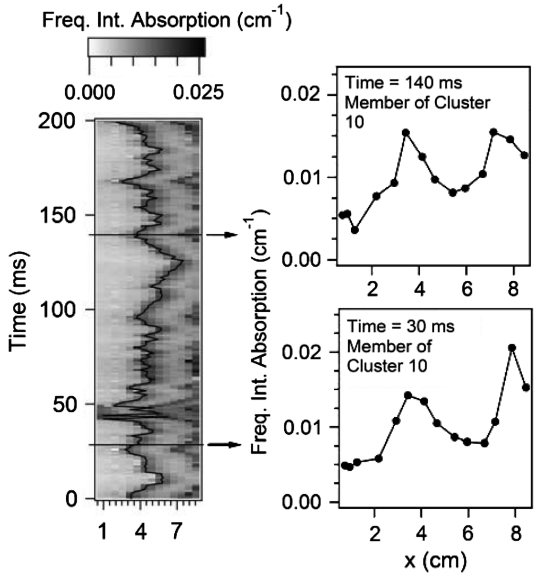

Fig. 6 Absorption-versus-time plot for one data segment from Fig. 5 when the shock is partially in the observation window. The solid black curve indicates the shock front. Also shown are two plots of the 14 LOS measurements at two particular instants of time when the shock front is at a similar location in the window.

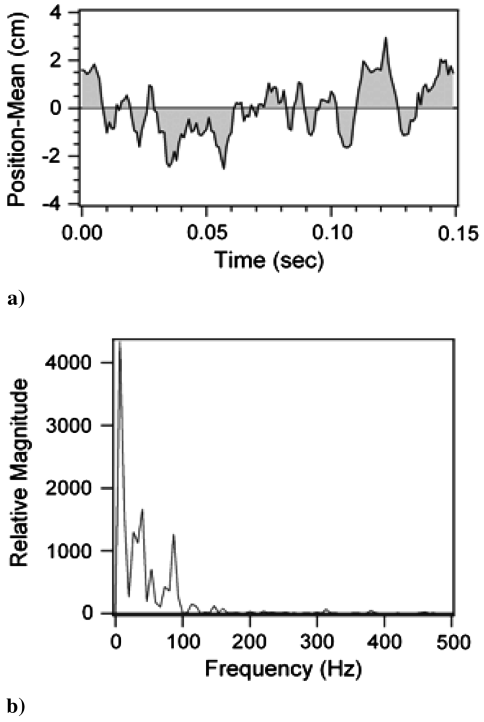

Fig. 7 Plots of a) position of the shock front relative to its mean position and b) power spectrum corresponding to the oscillations of the shock front.

obtained by just examining the power spectrum of a single LOS. In the case of a single LOS, it is not possible to know where the shock front is located: only the amplitude of the frequency-integrated absorption is available. As can be seen in Fig. 6, if one were to examine the frequency content of the LOS located near $x = 2$ cm, it would have frequency content very different from one located at $x = 4$ cm. In addition, the immunity to turbulent fluctuations of the flow will be much less than in the case of using a single LOS.

The subject of shock-train oscillations has only been studied in a limited manner, and much about the unsteadiness of these flows is still not understood [5]. However, several studies have examined the frequency and the amplitude of these oscillations [6,7]. In the case of the study by Ikui et al. [6], the peak-to-peak amplitude of the shock oscillations was found to be on the order of the equivalent duct diameter. Here, the data in Fig. 7 indicate that the peak-to-peak shock-front oscillations are approximately 4 cm. This is nearly the equivalent duct diameter (5.75 cm) for the 4×10 cm rectangular cross section of isolator, and so this result is in good agreement with Ikui et al. In addition, they found that the frequency oscillations consisted of several strong peaks of several tens of hertz and several hundreds of hertz. In the current study, most of the primary frequency content of the shock oscillations is contained in frequencies below 100 Hz; however, two–three smaller components are above 100 Hz.

V. Data Clustering

This section first describes the reason for using data clustering as well as going over the k-means algorithm that is used here. Then it applies the method to the experimental data and also relates the derived clusters to the mean backpressure observed at the back-pressure valve.

Figure 5 shows a grayscale image representing all of the absorption data for the 7185.6 cm^{-1} line collected for run AB conducted during the measurement campaign. This set of data is quite large, and although it is possible to identify features by looking at individual times, an automated technique is desired that can group similar data together to achieve an enhancement in signal-to-noise ratio as well as finding similar features. Here, the likeness of the different times depends on the shock location in the window. For example, a detailed examination of two different time images shown in Fig. 6 indicates that these correspond to similar shock locations in the window. Ideally, averaging together all times when the shock is at nearly the same position in the window will improve the signal-to-noise ratio and highlight the features of the shock train. Obviously, a sequential time average would grossly distort the discrete nature of the shock structure.

A variety of methods can be used to perform the sorting of the data set such as peak-finding. As mentioned previously, peak-finding works well if the first shock is present in the window but fails as this shock moves outside the window region and only higher-order shocks are present. Instead, data clustering, also known as vector quantization, has been used here to perform the selective averaging. A similar approach has also been used previously in the interpretation of large-eddy simulations [8]. The essential element of data clustering is to subdivide the data into classes. The members of these classes are determined to be most similar to each other based on a distance metric. The distance metrics that will be used in the following analysis are based on the Minkowski metric [2]:

$$d_p(\mathbf{x}_i, \mathbf{x}_j) = \left(\sum_{k=1}^{d} |x_{i,k} - x_{j,k}|^p \right)^{1/p} \tag{1}$$

where $\mathbf{x}_i$ and $\mathbf{x}_j$ are vectors in a d-dimensional space, and p is an exponent that defines the particular Minkowski metric. Here, $p = 2$ has been used, and it corresponds to the classical definition of the distance between vectors in three-dimensional space called the Euclidean distance. In addition, the $p = 1$ metric known as the Manhattan distance has been used as well, and it is the sum of absolute differences for each component of the vectors and will not be as dominated by outliers. A variety of clustering algorithms exist that can be used to cluster a data set [2]; however, one of the most common and widely available algorithms is the k-means method that is used here. The k-means algorithm can be described through the following four steps:

1) Choose k cluster centers through either random selection of k vectors (patterns) from the data set, random partitioning of the data set, or predefined vectors given by the user.

2) Assign each vector to the closest center using the distance metric.

3) Recompute the cluster centers by taking the mean of the current cluster members.

4) If convergence criteria are not met, go to step 2. Typical convergence criteria are no (or minimal) reassignment of patterns to new cluster centers or a minimal decrease in squared error.

As can be seen from the outline of this algorithm, it is a relatively simple algorithm, which is the reason for its popularity, and it is very computationally efficient, because its computational time scales in direct proportion to the number of clusters and the data set size. In addition to the distance metric, the outcome of the clustering algorithm will also be significantly influenced by the number of clusters that the user decides to use, as well as their initial seeding. So when deciding upon the optimal clustering strategy using the *k*-means technique, it is useful to perform multiple clustering approaches in which the number of clusters, initial seeding, and distance metric are varied for the data set under consideration. After these multiple approaches are used, physical understanding can be used to assess the optimal clustering of the data set. Here, in this problem, because much is known about the shock structure from CFD simulations as well as previous work that has been done on shock-train structures, it is straightforward to interpret the results. For more complex problems, a variety of validation measures as well as visualization techniques exist that can aid in determination of the optimal clustering strategy; however, they should only be used in conjunction with physical insight [9,10].

Figure 8 shows the data clusters that have been derived from Fig. 5 using the *k*-means algorithm. The vectors that have been used for data clustering are the 14-dimensional vectors corresponding to the frequency-integrated absorption for the 7185.6 cm^{-1} line for each line of sight. Here, the Euclidean distance metric was used, the initial seeding was done through random partitioning of the initial data set, and the termination criterion was that less than 0.1% of the members switched class membership. Each cluster in Fig. 8 is composed of an average of 100 or more members of the data set in Fig. 5. When using data clustering, it is important that the data set has a sufficiently large number of members so that the clustering can be performed. Here, the maximum number of clusters chosen was 20, which is much less than the 6000 members of the data set. The *k*-means algorithm has also been run in several different methods for this data set, including changing the number of class members and using the Manhattan distance instead of the Euclidean distance. In all cases, the general features of the shock train were always observed (i.e., clusters similar to C6–C13 are in the final data set); however, there can be some differences for finer-scale features such as C14–C17, as well as how the algorithm groups the data in clusters C1–C5 and C17–C20. One important observation is that the Manhattan distance metric tends to filter the data so that more clusters correspond to cases such as C14 and C15 than when the clustering was performed with the Euclidean distance (clusters C1 through C5 typically decrease in this case if the number is fixed at 20).

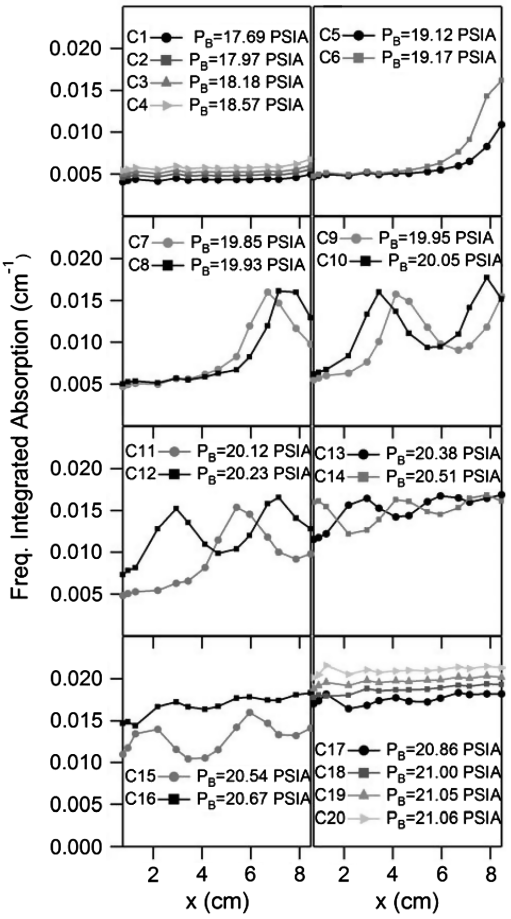

Fig. 8 Data clusters derived from the data set in Fig. 2. Clusters are ordered versus average backpressure.

The clusters have been presented as a function of average backpressure, which does a good job of ordering the clusters based on the shock position in the window. However, there are some discrepancies that are due to the method with which the average backpressure was determined. Calibrated diaphragm pressure transducers were used at two points located near the backpressure valve but were only sampled at 10 Hz. Because the absorption measurements were carried out at 1 kHz rates, this represents only a coarse measurement of backpressure. In addition, shock reflections near the measurement ports could also affect the measured backpressure. The correlation with the backing pressure is actually quite remarkable given that the backpressure differences between some clusters is less than 0.1 psia.

An additional characterization that can be easily applied is to look at the standard deviation present in the data used to form the cluster mean. Figure 9a shows cluster 10 along with error bars (not the standard errors) representing the standard deviation of the data used to form the cluster mean. This gives an indication of how the instantaneous results can vary from the mean value. The largest variations occur near the peaks of the shocks and can be expected because of the discrete nature of the spatial sampling with only 14 lines of sight. Also shown in Fig. 9b are two ways of computing the cluster average. In the first case, the spectra of the clusters have been averaged and then a Voigt-peak-fit routine has been used to determine the area, and in the second case, the integrated peak areas have been averaged. In Fig. 9b, the error bars for the integrated-then-averaged case are computed through the standard method of dividing the sample standard deviation by the square root of the number of samples, which is the standard deviation of the mean. In the case of the averaged-then-integrated case, the error bars correspond to the standard fit errors determined from the Hessian matrix. Note that in either case, very similar results are obtained and the sizes of the error bars are nearly equal as well. The averaged spectra are used to determine the static temperature and static pressure (from the line widths) in the next section. Ultimately, though, it is quite apparent from Figs. 7 and 8 that the clustering operation has yielded results compatible with known shock-train structures and CFD simulations. A more detailed comparison will be given in the rest of the paper.

VI. Path-Averaged Results

This section begins by examining what the cluster-averaged spectra look like and showing that it is possible to extract meaningful measurements of the path-averaged static pressure from them. It also shows that the cluster averaging preserves the pressure shift to the level of being able to resolve the streamwise profile of the shock train. Then the data is processed for the run conditions detailed in Sec. II, followed by a discussion of the quality of the data through such techniques as repeated runs.

As previously mentioned, the spectra for each cluster are averaged for each spectral region of interest. Figure 10a shows an example of what the averaged spectra look like both before and after the shock front for the absorption line centered at 7185.6 cm^{-1}. Both the peak areas and the line widths increase significantly in the higher-pressure and higher-temperature region after the shock. This shows that it is

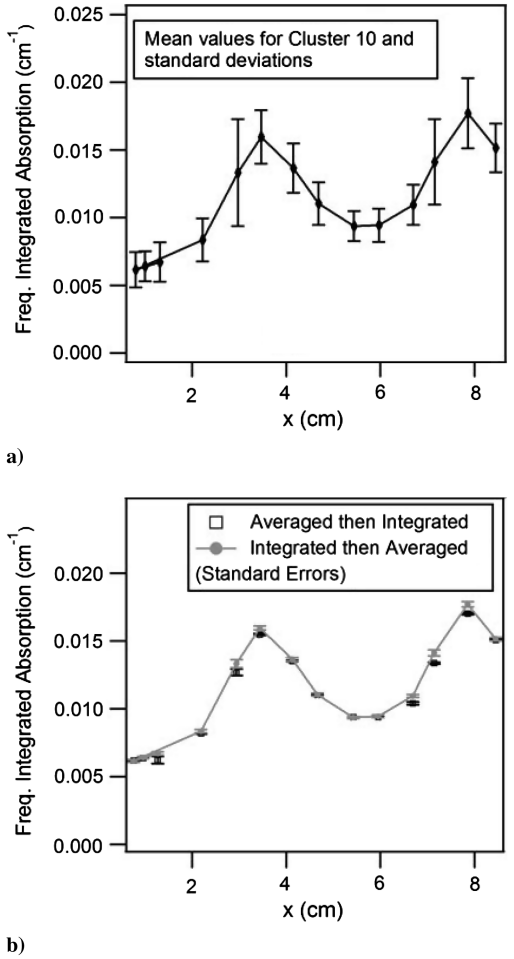

Fig. 9 Plots of a) average values for cluster 10 plus error bars representing the standard deviation (not the standard deviation of the mean) that illustrate the variability of the cluster data set and b) different methods of computing the cluster average along with standard error bars.

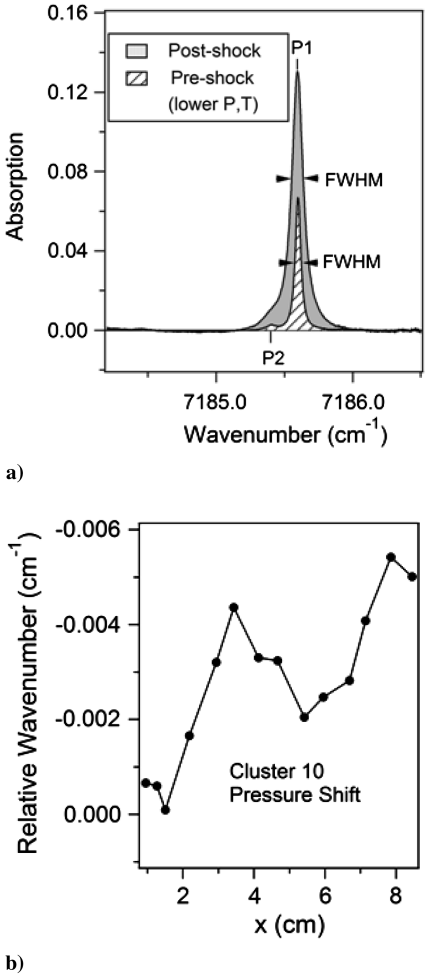

Fig. 10 Plots of a) cluster-averaged spectra for a LOS in front of the first shock and LOS after the shock front and b) the shift of the line center for cluster 10 (FWHM denotes full width at half-maximum).

possible to measure not only the temperature and water concentration of the flow, but also static pressure through knowledge of the collisional broadening parameters.

Also shown in Fig. 10b is the sensitivity of the line center position to pressure shifts that occur in the flow. The similarity between cluster 10 in Figs. 9 and 10b is good and similar results were found for other clusters in Fig. 8. Measurement of this quantity, though, requires the pressure-shift parameter be known as a function of temperature and gas composition. Currently, such measurements are only sparsely reported in literature and very little has been reported on the temperature dependence of this parameter, and so a full analysis has not been attempted here. Also, as can be seen in Fig. 2, not all of the LOS are perpendicular to the flow direction, which means a small Doppler-induced shift will occur. At a nominal flow velocity of 800 m/s and a tilt angle of 2 deg into the flow, the corresponding Doppler shift is 0.0007 cm^{-1}, and so these effects must also be taken into account. Finally, the changes in wave number (0.001 cm^{-1} or 30 MHz) that occur require accurate calibration of the frequency axis if quantitative results are to be obtained. In this experiment, an etalon with a free spectral range of 2.000 ± 0.002 GHz at 1550 nm was used, resulting in a frequency resolution better than (0.000007 cm^{-1} or 2 MHz). Because of the difficulty of these experiments, no further analysis of the pressure-shift data has been made, but the present results suggest that this could be used in more refined studies.

As previously discussed in Part 1 [1], a Boltzmann plot is used to obtain the temperature from the peak areas of four different spectral lines, and then this temperature is used to constrain the Voigt-peak-fitting algorithm to obtain a measure of the pressure broadening. The results of doing this for the clusters are shown in Figs. 11 and 12. The static temperatures and pressures that have been obtained are path-averaged in a direction largely perpendicular to the streamwise flow direction, as indicated in Fig. 2. This path-averaging is not a simple mass-weighted averaging of the flow quantities because of the presence of the exponential Boltzmann probabilities, and it is necessary to compute absorption maps such as Fig. 2 when comparing CFD computations. Because the data is path-averaged, it should not be interpreted as a measurement of the temperature or pressure at a particular point in the flow. However, the data reported here clearly capture the significant flow variations occurring in the streamwise direction. In fact, the path-averaging that takes place when collecting this data is the same as would occur when using a schlieren system to visualize the shock structure. The difference here is twofold. First, a schlieren system would typically illuminate the entire side view of the window and so a two-dimensional image would be formed. Here, hardware restrictions at the current time prevent us from implementing such an approach. However, in contrast to schlieren, it is much easier to derive quantitative measurement of path-integrated pressures, temperatures, and water concentrations, because they are directly related to absorption measurements. In schlieren, the total density is related to the derivative of the refractive index, and so obtaining quantitative measurements is very difficult in a noisy environment such as a shock train.

The variations or errors from the measured values reported here depend on multiple aspects when interpreting the results. First, and most straightforward, are the errors associated with fit errors of the absorption peaks. As can be deduced from Figs. 9b and 10a, these errors are quite small and are smaller than the symbol size in Figs. 11

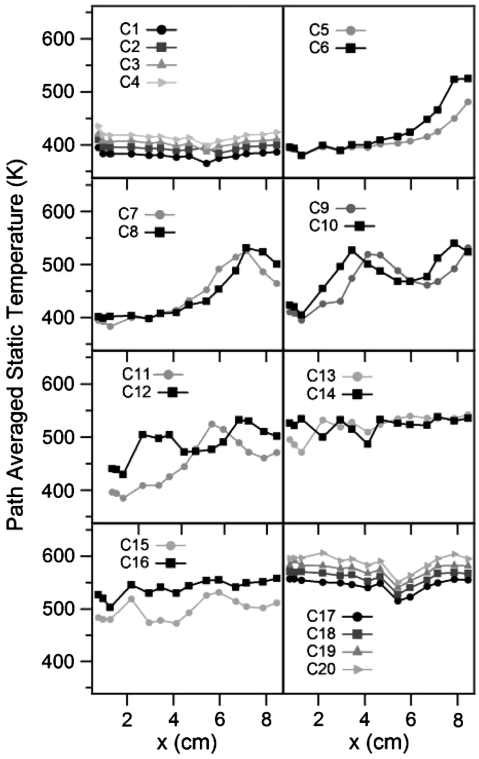

Fig. 11 Static temperature for the clusters from Fig. 6. Error bars derived from the curve-fit errors are smaller than the symbol size.

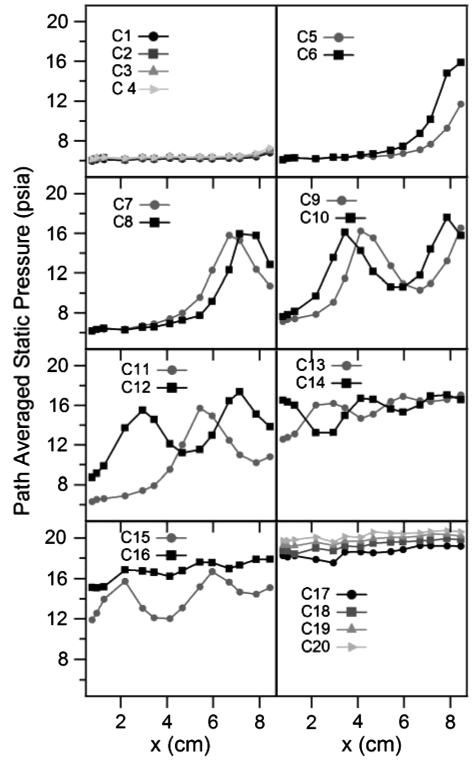

Fig. 12 Static pressures for the clusters from Fig. 6. Error bars are derived from the curve-fit errors are smaller than the symbol size.

and 12. In addition to these errors, there exist variations in the line parameters used to perform the Boltzmann plot as well as the broadening parameters used to determine the pressure broadening in the literature. Here, recent studies as well as the HITRAN 2004 database were used [11–14]. These sources can vary by several percent and so necessarily will impact the absolute accuracy. This error can be propagated through the Boltzmann plots and Voigt fits to obtain estimates on the absolute accuracy, as done in Part 1 [1]. These issues can also be addressed by comparing with known measurements, as was done in Part 1, which found the TDLAS measurements for the Mach 2 flow case to be in agreement with known standards to within 2%. The final sources of error involve the clustering process itself. Because it is an averaging process, Figs. 11 and 12 present the mean flow quantities. As can be seen in Fig. 9a, the instantaneous flow properties can vary significantly from these values. However, only comparison of mean flow values with computations as well as literature is currently possible, because of the difficulty in doing time-dependent calculations or measurements. In this case, the issue is how the statistical variation of the flow affects the cluster average. To address this question, the run-to-run variability in the measurements was determined, as shown in Fig. 13 for cluster 10. Because runs AB and AF (and, in a similar fashion, AC and AG) have inflow properties similar to the isolator, as shown in Table 1, they can be compared on a point-to-point basis for static temperature and pressure. Runs AB and AC were separated by several hours from runs AF and AG on the night that the measurements were being made. Both sets of runs used facility air heated to different initial temperatures, thereby requiring different amounts of vitiation to reach the same total enthalpy required for the run condition. Different amounts of vitiation result in significantly different water concentrations in the flow. As Fig. 13 shows, the agreement between runs is excellent for cluster 10 and suggests that the results are not dependent on the amount of water present in the flow; that is, the measured static temperatures and pressures are functions of the flow conditions. The average variation for the temperature measurements is approximately 3% and for the case of the static pressure is 5%. This variation will depend on the particular cluster for which the run-to-run variability is being tested; however, the numbers determined here are quite indicative of clusters C5–12, in which the major variations of the shock are present. Also note that some of this variability is not just due to the measurement process. The facility air supply, natural-gas-flow controller, and the oxygen-mass-flow controller exhibit an oscillation of approximately 1–2% that could be partially responsible for the variations. Nevertheless, it is quite remarkable that the measurements are so repeatable given the complexity of the measurement environment.

VII. Discussion

The path-averaged measurements in the previous section can be compared with wall pressure measurements, the literature on shock-train structures, and CFD simulations of the flow. Before examining the results in detail, it is important to review what are known to be the key parameters that influence the formation of the shock train. A shock train forms inside of a duct instead of a single normal shock wave, because of the interaction between the shock wave and the boundary layer along the wall surface [5,15–18]. This type of interaction is strongly governed by the Mach number of the flow and the confinement factor δ/h, where δ is the undisturbed boundary-layer thickness and h is the duct half-height [5]. The shock train has been shown to transition from the ideal normal shock to a normal shock train and then to an oblique shock train as the confinement parameter and the Mach number increase with the transition to an oblique shock train occurring for Mach numbers of 1.8–2.2, depending on the flow confinement parameter [5,15,19]. In the particular case under consideration here, the boundary-layer thickness at the foot of the shock was not experimentally available with the current setup. However, CFD simulations discussed later can be used to place a lower bound of 0.3 on the confinement factor. The reason that this is taken as a lower bound is that these simulations did not include any surface roughness. However, the surface is rough here, due to a thermal barrier coating that is used to protect isolator walls during hot run conditions [20]. In addition, measurements of the boundary-layer thickness at different points in the isolator during situations in which no backpressure is present have found that the CFD simulations often underestimate its thickness [21]. This confinement factor combined with the Mach number of the incoming

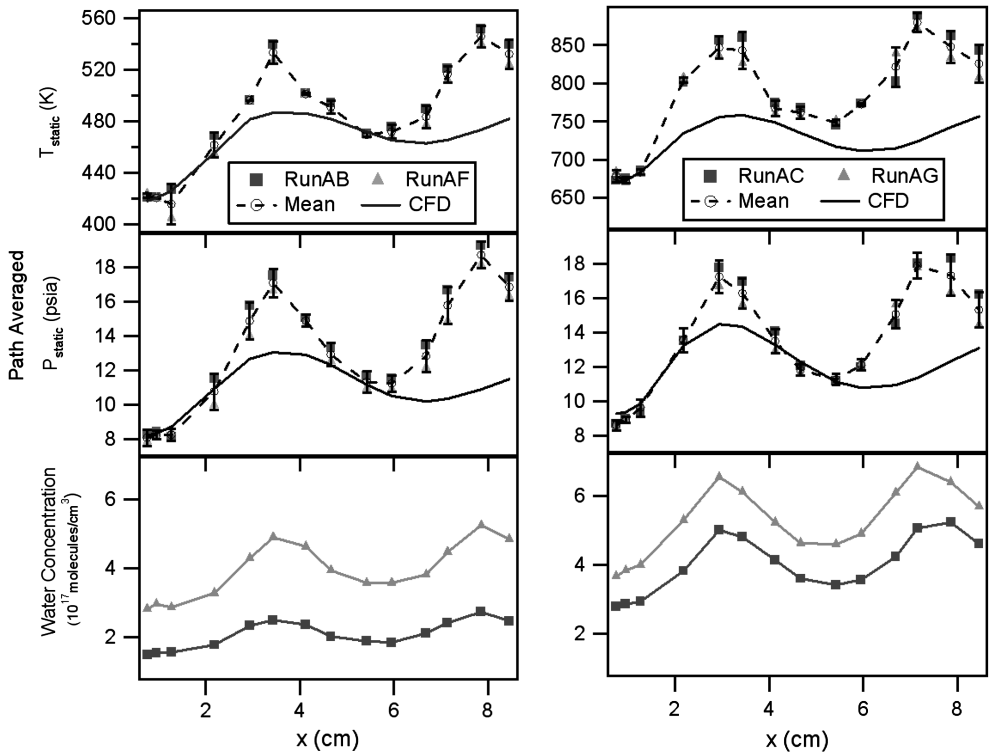

Fig. 13 Run-to-run variations in measured quantities for cluster 10: a) runs AB and AF and b) runs AC and AG. The error bars are based on the standard deviation of values between similar runs. Also shown are the path-averaged measurements derived from the CFD simulation with the cubic turbulence model in Fig. 15.

flow being nearly 2.2 indicates that the observed shock train is likely oblique. The sequence of shocks is known to form in the core flow due to an aerodynamic nozzle effect in which the boundary layer effectively forms converging and diverging nozzles that can accelerate the flow after a shock [5,16]. Therefore, the shock spacing is directly related to the shape of the turbulent boundary layer and so measurements of the spacing such as conducted here can provide a sensitive probe of turbulence models used in modeling scramjet isolators as well as other applications of supersonic duct flows. Many more details about shock-train structure can be found in the excellent review by Matsuo et al. [5] that will not be repeated here.

A. Comparison with Wall Pressure Measurements

Most early measurements of shock-train structures focused on wall pressure measurements (often time-averaged), which are relatively easy to conduct. Because of this, a wealth of information exists on shock-train structures in the literature that relies on these types of measurements [5]. Figure 14 shows the wall pressure measurements in the isolator at one particular time during the course of run AB. In this case, the shock front is located a considerable distance upstream in the isolator. As is typically the case for wall pressure measurements, little or no oscillations are observed as the pressure rises from the foot of the shock [5]. This is because the pressure measurements are insulated from the oscillations occurring in the core flow region by the boundary layer. In contrast to this, the absorption measurements are sensitive to the pressure changes that are occurring along the entire width of the isolator and are therefore going to most strongly reflect the changes in the core flow region. This is the reason that the shock oscillations are clearly observed in Figs. 11 and 12. A final aspect that can be inferred from Fig. 14 is the comparison of the asymptotic values being measured in the shock train. For example, as already discussed in Part 1 [1], the pressure in the Mach 2 flow case agrees with the pressure transducer measurements to an accuracy of 3%. Here, this good agreement can be seen by comparing the static pressure at $x < 10$ cm of the shock in Fig. 13 with the static pressure of cluster 1 in Fig. 10. In addition, if

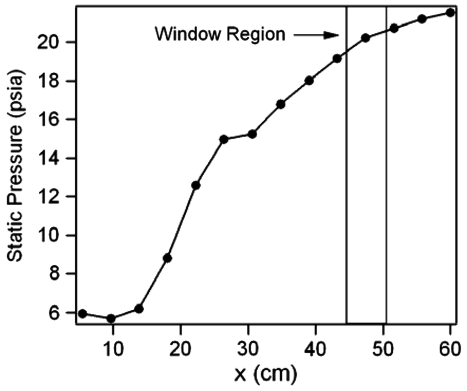

Fig. 14 The static pressure across the isolator from wall pressure measurements. The two vertical lines indicate the position of the optical probing window.

the shock front is at its maximal distance forward in the isolator, then the pressure in the window region will be approximately 21 psia. This is in good agreement with cluster 20, for which the average pressure from all 14 paths is 19.3 psia and represents a disagreement of 8%. These two points (along with the computed mole percent, as detailed in Part 1 for the Mach 2 flow) provide the best independent measures of the absolute accuracy of the measurements.

B. Comparison with Computational Fluid Dynamics Simulations

One of the goals for TDLAS measurements within our research group is to use them to help validate CFD models that are being used to model supersonic flows. The reason for this interest is the potential of TDLAS to provide in-flight information about the inflow properties of the engine as well as providing routine ground-based diagnostics. Although it is limited by its line-of-sight nature, significant information can still be gained through detailed

comparisons with CFD, as will be discussed here for the case of the shock train.

For this particular experiment, multiple simulations have been employed that vary the backpressure condition as well as the turbulence model within CFD + +, which is a general-purpose CFD tool developed by Metacomp Technologies [22]. CFD + + uses a finite volume numerical framework, with multidimensional total-variation-diminishing schemes and Riemann solvers for accurate representation of supersonic flows. Several types of Riemann solvers are available; the Harten–Lax–van Leer–contact Riemann solver with minmod flux-limiting was used in the simulations described here. Multigrid acceleration is available to provide a fast and accurate solution methodology for both steady and unsteady flows. A variety of one-, two-, and three-equation turbulence models are available for Reynolds-averaged Navier–Stokes (RANS) calculations, along with large-eddy simulation (LES) and hybrid RANS/LES options. Unless otherwise specified, turbulence was modeled using the two-equation cubic κ-ε model. This model has nonlinear terms that account for normal-stress anisotropy, swirl, and streamline curvature effects. At solid surfaces, an advanced two-layer wall function with equilibrium and nonequilibrium blending was employed to reduce grid requirements. The code supports both structured (quadrilateral and hexahedral) and unstructured (triangle, prism, and tetrahedral) grids. A message-passing interface is used to take advantage of modern parallel-processing computers. The numerical solutions were considered to be converged based on the residual history and the steadiness of the mass-flow rate. The mass-flow rate should not change: that is, it should be constant along the isolator.

The numerical simulation was based on the rectangular isolator test configuration in the AFRL/RZAS research cell 18 supersonic wind tunnel. This is a direct-connect facility; that is, the isolator test section is connected to the exit of the facility nozzle. The numerical simulations were extended from the facility nozzle plenum to the entrance of the isolator test section to provide the inflow conditions for the isolator section. This practice obviates the need for ad hoc profiles at the isolator entrance. The exit of the isolator section was pressurized to create a choking condition in the isolator. Various backpressure conditions were imposed to create a shock-train system in the isolator. A no-slip adiabatic boundary condition was imposed on the isolator walls. Because the isolator was assumed to be symmetric along the centerline plane, only half of the plane was computed in this study. The computational domain consisted of 768,000 grid cells. The grid was clustered to all solid surfaces at a level appropriate for the use of wall functions ($y+ \leq 30$).

As can be seen in Fig. 15, both cubic and realizable κ-ε turbulence models yield very similar shock structures in the plane that is being probed. There are slight differences between the shock anchoring points, and the realizable turbulence model yields a slightly smaller spacing between the first and second shocks (7.8 vs 8.3 cm for the peaks on the isolator centerline). It is quite clear from Figs. 13 and 15 that the measurements indicate smaller shock spacing ($\sim$4.3 cm) than the computations. However, an exact comparison requires that the absorption maps are computed as shown in Fig. 1, and the results are then path-averaged in the correct manner. The results of this can be seen in Fig. 13, which shows the path-averaged data computed from the cubic κ-ε turbulence model shown in Fig. 15. To do this comparison, the window must be shifted to a location such that the first shock overlaps with measured data. This is a well-known problem in comparing CFD results with experimental data for shock-train structures [5,17]. In addition to shifting the observation window, it is possible to photographically scale the CFD to reduce the shock spacing. If this is done, it is found from clusters C9, C10, C12, and C15 that the CFD must be shrunk by a factor of 0.55 (i.e., the CFD overestimates the spacing by 45%) in the case of the cubic κ-ε turbulence model and by a factor of 0.62 for the realizable κ-ε turbulence model. Additionally, Fig. 13 shows that the variations in both path-averaged temperature and pressure are more significant than computed in the CFD simulations. In particular, the temperature difference between the first shock peak to the trough immediately following it is from 2–2.6 times greater in the case of the measurements, and for the static pressure, the measurements show a variation that is 1.6–2 times greater than the CFD computation. The first instinct is to assume that this means that the shock structures are more intense than predicated by the calculations. However, this may not be the case, because the measurements are path-averaged. For example, it is possible that shock is wider than indicated in Fig. 15, and this would lead to a larger path-integrated temperature and pressure. Unfortunately, the measurement geometry in Fig. 1 is not very sensitive to changes in the transverse direction, and so a definitive answer to this question is not possible with the current experimental setup.

That the CFD computation is not in agreement with the measurements is not surprising given prior works that have attempted to match CFD simulations to shock-train structure. One of the most detailed studies by Carroll et al. [17] compared inflow measurements of a normal shock train made using laser Doppler velocimetry with simulations using the Baldwin–Lomax turbulence model and the Wilcox–Rubesin turbulence model. Although both turbulence models are thought to be not as good as the more modern ones used in the preceding simulations, the Wilcox–Rubesin calculation captured the shock-train structure well in the sense that the Mach number contours agreed closely with the velocimetry measurements. However, the Wilcox–Rubesin model and the Baldwin–Lomax did not match the measured wall pressure rise. In that study, no inflow measurements were made. It is also important to realize in that case that the authors were dealing with a normal shock-train structure that was relatively steady, because the inflow Mach number was 1.6 as opposed to 2.2 in the current study. Here, unlike the case of Carroll et al., the change in turbulence model made very little difference in improving the agreement of the CFD simulations with the measured

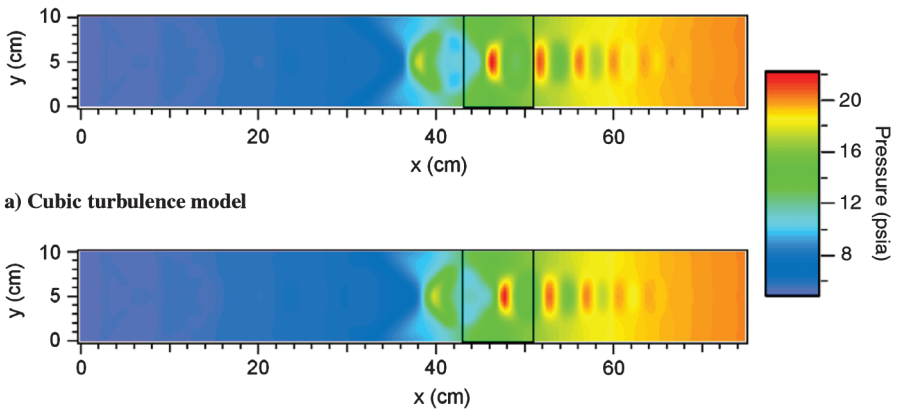

Fig. 15 A pseudo color plot of the static pressure computed using CFD + + with two different turbulence models for a uniform backpressure of 19.89 psia. Also shown is the optical observation region indicated by the blck rectangle.

data. This could be due to several more significant factors. One problem that is well known is the influence of the surface roughness of the thermal barrier coating. Previous efforts to model this surface roughness correctly have not yielded satisfactory results, and using an approximation that the isolator duct is smooth is clearly not correct. This will influence the boundary-layer thickness and its turbulence characteristics so that it can clearly influence the structure of the shock train. Another aspect that has been raised in the literature is that the computations done here, as well as the majority of simulations of shock trains, involve the use of Reynolds-averaged Navier–Stokes codes [5]. The problem is that the unsteady nature of the shock oscillations, as discussed in Sec. IV cannot be captured properly by the turbulence models using a Reynolds-averaged code, and therefore such methods as large-eddy simulations or direct numerical simulations are required to properly simulate the flow. This problem will be more significant at higher Mach numbers, because the flow unsteadiness increases substantially. In conclusion, the disagreement between experiment and simulation is likely due to a combination of factors: turbulence modeling, surface roughness, and flow unsteadiness. Closing the gap between experiment and simulation will require improvements on both fronts.

VIII. Conclusions

To our knowledge, this represents the first time-resolved (millisecond) and spatially (5 mm) resolved inflow measurements of static temperature, static pressure, and density of a supersonic isolator shock train. In addition, this study represents one of the largest simultaneous tunable diode laser absorption experiments that has been performed at similar supersonic combustion facilities, with 16 paths sampled over 3 spectral regions (48 spectra) at rates greater than 1 kHz. This work lays the groundwork for understanding the effects of shock-train structure on TDLAS-based mass-flux sensors as well as improving fundamental understanding of the flow physics of these shock structures. This study used a backpressure valve to generate the shock train, but this approach can be applied to the study of precombustion shock-train amplitude and frequency instabilities resulting from combustion. It was found that the shock train oscillates with a peak-to-peak amplitude of approximately 4 cm, with a power spectrum with significant frequency components below 100 Hz. This is in good agreement with previous studies of shock-train oscillations. The use of data clustering allowed substantial insight into the shock structure to be made even though the flow was quite unsteady. This enabled RANS CFD simulations to be compared with the cluster averages. Here, it was found that despite the lack of complication of the shock train being produced by combustion, an apparent discrepancy regarding the streamwise shock spacing exists. This discrepancy is clearly established because of the good experimental spatial resolution in the streamwise direction. In addition, the variations in path-averaged temperature and static pressure are found to be approximately a factor of 2 greater than predicted. Although the exact sources of the differences are not known, it is quite likely that they are due to some combination of three factors: inadequate surface roughness model, problems in the RANS turbulence model, and the unsteady nature of the flow. Nevertheless, these results show that TDLAS has the potential to observe complex spatiotemporal oscillations in supersonic flows and then allow comparisons with CFD simulations to be made. Although it may not be the first choice for studying shock-train structures (schlieren and velocimetry are the classics), it may be the only technique that offers the ability to study these structures in a practical manner in a flight vehicle, because it can be readily miniaturized.

Acknowledgments

This work was supported by the U.S. Air Force Office of Scientific Research (Michael Berman, Program Manager), and C. D. Lindstrom was sponsored under a National Research Council Fellowship. The authors thank William Terry for his assistance in hardware design and setup as well as the RC18 test team (Matt Streby, Steven Lin, Steve Ennekin, Paul Kennedy, and Keven Jackson) for rig operation.

References

[1] Lindstrom, C. D., Jackson, K. R., Williams, S., Givens, R., Bailey, W. F., Tam, C.-J., and Terry, W. F., "Shock-Train Structure Resolved with Absorption Spectroscopy Part 1: System Design and Validation," *AIAA Journal*, Vol. 47, No. 10, Oct. 2009, pp. doi:10.2514/1.41074

[2] Jain, A. K., Murty, M. N., and Flynn, P. J., "Data Clustering: A Review," *ACM Computing Surveys*, Vol. 31, No. 3, 1999, pp. 264–322. doi:10.1145/331499.331504

[3] Igor Pro, Software Package, Ver. 6.0, Wavemetrics, Inc., Lake Oswego, OR, 2007.

[4] Venetsanopoulos, I. P. A., "Median Filters," *Nonlinear Digital Filters: Principles and Applications*, Springer–Verlag, New York, 1990, pp. 63–112.

[5] Matsuo, K., Miyazato, Y., and Kim, H.-D., "Shock Train and Psuedo-Shock Phenomena in Internal Gas Flows," *Progress in Aerospace Sciences*, Vol. 35, No. 1, 1999, pp. 33–100. doi:10.1016/S0376-0421(98)00011-6

[6] Ikui, T., Matsuo, K., Nagai, M., and Honjo, M., "Oscillation Phenomena of Pseudo-Shock Waves," *Bulletin of the JSME*, Vol. 17, No. 112, 1974, pp. 1278–1285.

[7] Sugiyama, H., Takeda, H., Zhang, J., Okuda, K., and Yamagishi, H., "Locations and Oscillation Phenomena of Pseudo-Shock Waves in a Straight Rectangular Duct," *JSME International Journal, Series B (Fluids and Thermal Engineering)*, Vol. 31, No. 1, 1988, pp. 9–15.

[8] Usera, G., Vernet, A., Pallars, J., and Ferre, J. A., "A Conditional Sampling Method Based on Fuzzy Clustering for the Analysis of Large-Scale Dynamics in Turbulent Flows," *European Journal of Mechanics, B/Fluids*, Vol. 25, No. 2, 2006, pp. 172–191. doi:10.1016/j.euromechflu.2005.06.002

[9] Halkidi, M., Batistakis, Y., and Vazirgiannis, M., "Clustering Validity Checking Methods: Part 2," *SIGMOD Record*, Vol. 31, No. 3, 2002, pp. 1–9.

[10] Vesanto, J., "Neural Network Tool for Data Mining: SOM Toolbox," *Proceedings of Symposium on Tool Environments and Development Methods for Intelligent Systems (TOOLMET2000)*, Univ. of Oulu, Oulu, Finland, 2000, pp. 184–196.

[11] Delaye, C., Hartmann, J.-M., and Taine, J., "Calculated Tabulations of H_2O Line Broadening by H_2O, N_2, O_2, and CO_2 at High Temperature," *Applied Optics*, Vol. 28, No. 23, 1989, pp. 5080–5087. doi:10.1364/AO.28.005080

[12] Durry, G., Zeninari, V., Parvitte, B., Barbu, T. L., Lefevre, F., Ovarlez, J., and Gamache, R. R., "Pressure-Broadening Coefficients and Line Strengths of H_2O Near 1.39 μm: Application to the in Situ Sensing of the Middle Atmosphere with Balloonborne Diode Lasers," *Journal of Quantitative Spectroscopy and Radiative Transfer*, Vol. 94, Nos. 3–4, 2005, pp. 387–403. doi:10.1016/j.jqsrt.2004.09.033

[13] Rothman, L. S., Jacquemart, D., Barbeb, A., Benner, C. D., Birkd, M., Browne, L. R., et al., "The HITRAN 2004 Molecular Spectroscopic Database," *Journal of Quantitative Spectroscopy and Radiative Transfer*, Vol. 96, No. 2, 2005, pp. 139–204. doi:10.1016/j.jqsrt.2004.10.008

[14] Liu, X., Zhou, X., Jeffries, J. B., and Hanson, R. K., "Experimental Study of H_2O Spectroscopic Parameters in the Near-IR (6940–7440 cm^{-1}) for Gas Sensing Applications at Elevated Temperature," *Journal of Quantitative Spectroscopy and Radiative Transfer*, Vol. 103, No. 3, 2007, pp. 565–577. doi:10.1016/j.jqsrt.2006.07.008

[15] Carroll, B. F., and Dutton, J. C., "Characteristics of Multiple Shock Wave/Turbulent Boundary-Layer Interactions in Rectangular Ducts," *Journal of Propulsion and Power*, Vol. 6, No. 2, 1990, pp. 186–193. doi:10.2514/3.23243

[16] Carroll, B. F., and Dutton, J. C., "Multiple Normal Shock Wave/Turbulent Boundary-Layer Interactions," *Journal of Propulsion and Power*, Vol. 8, No. 2, 1992, pp. 441–448. doi:10.2514/3.23497

[17] Carroll, B. F., Lopez-Fernandez, P. A., and Dutton, J. C., "Computations and Experiments for a Multiple Normal Shock/Boundary-Layer Interaction," *Journal of Propulsion and Power*, Vol. 9, No. 3, 1993, pp. 405–411. doi:10.2514/3.23636

[18] Om, D., and Childs, M. E., "Multiple Transonic Shock-Wave/Turbulent

Boundary-Layer Interaction in a Circular Duct," *AIAA Journal*, Vol. 23, No. 10, 1985, pp. 1506–1511. doi:10.2514/3.9117

[19] Waltrup, P. J., and Billig, F. S., "Structure of Shock Waves in Cylindrical Ducts," *AIAA Journal*, Vol. 11, No. 10, 1973, pp. 1404–1408. doi:10.2514/3.50600

[20] Lin, K.-C., Tam, C.-J., Boxx, I., Carter, C., Jackson, K., and Lindsey, M., "Flame Characteristics and Fuel Entrainment Inside a Cavity Flame Holder in a Scramjet Combustor," AIAA Paper 2007-5381, July 2007.

[21] Lin, K.-C., Tam, C.-J., Jackson, K. R., Eklund, D. R., and Jackson, T. A., "Characterization of Shock Train Structures Inside Constant-Area Isolators of Model Scramjet Combustors," AIAA Paper 2006-0816, January 2006.

[22] CFD + +, Software Package, Ver. 6.1, Metacomp Technologies, Agoura Hills, CA, 2006.

R. Lucht
Associate Editor